Materials Advances

ROYAL SOCIETY OF CHEMISTRY

PAPER

View Article Online
View Journal

Cite this: DOI: 10.1039/d6ma00373g

Double-network PEDOT:PSS xerogel fibers with high stretchability and electrical stability for wearable strain sensing

Gayaneh Petrossian,[a] Sara Ebrahimi,[a] Floriane Miquet-Westphal,[a] Hang Xu[b] and Fabio Cicoira *[a]

Received 17th March 2026,
Accepted 7th May 2026

DOI: 10.1039/d6ma00373g

rsc.li/materials-advances

Conductive polymer xerogels provide a promising route toward mechanically stable and water-independent alternatives to conventional hydrogels for wearable bioelectronics. However, achieving high stretchability, mechanical robustness, and stable electrical performance in xerogel fibers remains challenging. Here, we develop highly stretchable and conductive double-network PEDOT:PSS xerogel fibers fabricated through freeze–thaw-induced physical crosslinking of poly vinyl alcohol (PVA) followed by borax-mediated crosslink formation. The resulting fibers exhibit enhanced network integrity and mechanical robustness, enabling tensile strength up to ~16 MPa and elongation at break exceeding 1100% at an optimized borax concentration, while maintaining stable electrical conductivity (~0.8 S m^{-1}). The fibers display reproducible strain-dependent resistance changes with gauge factors up to ~19 at high strain. When integrated as wearable sensors, the xerogel fibers enable reliable real-time monitoring of human motion, including finger, wrist, and elbow movements. This double-network xerogel strategy provides a simple and scalable approach to engineering mechanically robust conductive fibers for next-generation wearable sensing and bioelectronic applications.

Introduction

Flexible and stretchable conductive materials composed of conductive polymers and elastic matrices are increasingly explored for applications in wearable health monitoring, implantable bioelectronics, and human–machine interfaces.[1–10] Conducting polymer-based hydrogels have attracted significant attention due to their combination of softness, stretchability, and ionic/electronic conductivity. Among these materials, poly(3,4-ethylenedioxythiophene):polystyrene sulfonate (PEDOT:PSS) has emerged for its tunable electrical conductivity, aqueous processability, biocompatibility, and potential for self-healing. However, in its pristine form, PEDOT:PSS generally exhibits moderate conductivity (~1 S cm^{-1}) and limited stretchability (~5%).[11,12] Moreover, most PEDOT:PSS-based hydrogel conductors remain strongly dependent on water content to maintain their mechanical compliance and electrical performance, making them vulnerable to dehydration, dimensional instability, and long-term performance degradation in ambient environments. To overcome these limitations, various additives have been introduced. Small-molecule polyols such as glycerol,[13] ethylene glycol (EG),[14] and xylitol[15] primarily act as conductivity enhancers, while polymeric additives such as polyvinyl alcohol (PVA),[16] polyurethane (PU),[17] polyurethane diol (PUD),[18] and polyethylene glycol (PEG)[19] are commonly incorporated to improve mechanical compliance, stretchability, and structural stability of the conductive network.

Xerogels, the dry analogs of hydrogels, are polymer networks obtained by removing water from a hydrogel while preserving the underlying crosslinked structure. Unlike aerogels, which require supercritical drying to maintain an open-pore architecture, xerogels are typically produced through ambient drying or mild thermal drying, making them simpler and more cost-effective to manufacture.[20] The removal of water results in a denser and mechanically stable material that is no longer dependent on hydration for structural integrity. Consequently, xerogels overcome key limitations of hydrogels, including dehydration, dimensional instability, and degradation of mechanical and electrical performance over time. These advantages make conductive xerogels particularly attractive for wearable and bioelectronic applications requiring stable performance under ambient conditions.

To enhance the mechanical performance of polymer-based hydrogels and xerogels, both physical and chemical crosslinking methods have been employed.[21,22] Physical crosslinking

[a] Department of Chemical Engineering, Polytechnique Montréal, Montréal, Québec H3C 3A7, Canada. E-mail: fabio.cicoira@polymtl.ca
[b] Department of Mechanical, Industrial and Aerospace Engineering, Concordia University, Montréal, Québec H3A 0C3, Canada

methods, such as freeze–thaw cycling,[23] rely on non-covalent interactions, including hydrogen bonding and crystallite formation, to establish network structures without the introduction of additional chemicals. In PVA systems, freeze–thaw processing promotes the formation of microcrystalline domains that serve as physical junction points, resulting in enhanced elasticity and mechanical strength.[24] Chemical crosslinking involves the formation of covalent or reversible bonds using crosslinkers such as glutaraldehyde,[25] citric acid,[26] or borax.[27–29] Borax forms reversible di-diol complexes with PVA chains, enabling dynamic and tunable mechanical behavior.[30] Combining both physical and chemical crosslinking approaches can therefore produce hybrid networks that balance flexibility, strength, and structural stability.[31,32]

Conductive fibers are particularly attractive for wearable sensing applications due to their inherent flexibility, lightweight nature, and ability to conform to complex and dynamic surfaces.[33–35] Compared with bulk films, fiber-shaped sensors can accommodate larger deformation, provide improved mechanical compatibility with soft tissues, and enable reliable signal acquisition during motion. Fiber geometries also facilitate the integration into wearable platforms, such as textiles and skin-mounted devices. For example, fiber-like conductive hydrogels fabricated through freeze–thaw processing and weaving strategies have been reported as mechanically robust and stretchable sensors for human motion monitoring.[36] Similarly, PEDOT:PSS/PVA hydrogel fibers have demonstrated high mechanical strength and sensitivity for physiological sensing applications.[37] Despite these advances, developing conductive xerogel fibers that simultaneously exhibit high mechanical robustness, large stretchability, and stable electrical performance remains challenging, particularly in water-independent systems.

Here, we report highly stretchable and conductive double-network PEDOT:PSS xerogel fibers for wearable strain sensing applications. The fibers are fabricated through a double-network design combining freeze–thaw-induced physical crosslinking of PVA with borax-mediated dynamic crosslink formation. This strategy produces mechanically robust and electrically stable xerogel fibers that operate under water-independent conditions, addressing a key limitation of conventional PEDOT:PSS hydrogel strain sensors. By varying the borax concentration, the crosslink density can be systematically tuned, enabling control over the mechanical and electromechanical properties of the fibers. The resulting xerogel fibers exhibit tensile strains exceeding 1100% while maintaining stable electrical conductivity and reliable strain-dependent resistance changes. When integrated as wearable sensors, the fibers enable accurate real-time monitoring of human motion, demonstrating their potential for robust wearable bioelectronic applications.

While PEDOT:PSS/PVA-based systems and double-network hydrogels have been widely explored, most studies focus on hydrated materials whose performance depends on water retention. In contrast, this work focuses on conductive xerogel fibers, enabling water-independent operation while maintaining high mechanical robustness and electromechanical functionality. The integration of freeze–thaw-induced physical crosslinking with borax-mediated dynamic crosslinking results in a double-network structure that provides a favorable balance between strength, extensibility, and electrical stability in the dry state.

Materials and methods

Materials

Poly(vinyl alcohol) (PVA, 89 000–98 000 average molecular weight and 99+% hydrolyzed), glycerol (≥99.0%), and sodium tetraborate decahydrate (borax, ≥99.5%) were purchased from Millipore Sigma (St. Louis, MO, USA). PEDOT:PSS dispersion (conductive grade, SKU 483095, 1.3 wt% solids) was purchased from Millipore Sigma (St. Louis, MO, USA). Silicone elastomer Ecoflex Gel was purchased from Smooth-On (Macungie, PA, USA). Copper tape (88.9 μm, 10 mΩ sq^{-1}) was purchased from McMaster-Carr. The glass capillary tubes with an inside diameter of 1 mm were supplied by Iouyup (China).

Xerogel preparation

Initially, a 15 wt% aqueous solution of polyvinyl alcohol was prepared by dissolving PVA in ultrapure deionized (DI) water (18.2 MΩ cm at 25 °C) in an oil bath at 90 °C with continuous stirring for 2 hours until a clear solution was obtained. A precursor solution was prepared by mixing 1 g of the PVA solution, 1 g of PEDOT:PSS dispersion, and 0.1 g of glycerol under magnetic stirring at 50 °C for 5 min.

After thorough mixing, the homogeneous solution was injected using a syringe into molds with desired shapes, where the mold geometry defined the final form of the xerogel. For the preparation of the fibers, the mixture was injected into glass capillary tubes with an inside diameter of 1 mm and a length of 10 cm. For certain characterization techniques, films were also prepared by casting the solution into flat molds to obtain xerogel films with uniform thickness. Consequently, the materials were subjected to freeze–thaw (F–T) processing, consisting of freezing at −80 °C for 8 h followed by thawing at room temperature for 30 minutes, repeated for five cycles, resulting in physically crosslinked hydrogels. After freeze–thaw treatment, the samples formed fully solid, self-supporting structures that could be easily removed from the molds without deformation or damage. These samples were designated PPG. Following gel formation, the hydrogels were immersed for 30 s in aqueous borax solutions (concentrations of 0, 0.1, 0.25, and 0.5 M), followed by ambient drying to obtain the xerogels. For comparison, cast-only (CO) control samples were prepared by casting the precursor solution into films and allowing them to dry at room temperature without undergoing freeze–thaw treatment. Because no crosslinking occurred under these conditions, the materials did not form stable fibers. These samples were designated CO-PPG.

Characterization

The morphology of the xerogels was analyzed using a Quattro (Thermo Scientific) scanning electron microscope (SEM). The

samples were cryo-fractured using liquid nitrogen to achieve a clean representative cross-section of their internal structure.

The thermal stability of the xerogels was evaluated using thermogravimetric analysis (TGA, 5500, TA Instruments, USA). Measurements were performed in an open platinum crucible from 40–600 °C with a heating rate of 20 °C min^{-1}, under a nitrogen atmosphere (40 mL min^{-1}). Differential scanning calorimetry (DSC, Q2000, TA Instruments, USA) was used to determine the crystallinity percentage (X_c), using the following equation:

$$X_c = \frac{\Delta H_f}{\Delta H_f^{100}} \times 100 \quad (1)$$

where ΔH_f is the heat of fusion, measured by the area under the melting peaks in DSC, and ΔH_f^{100} is the heat of fusion for a 100% crystalline PVA, obtained from the literature (ΔH_f^{100} = 161.4 J g^{-1}).[38]

To study the chemical structure and bond formations, Fourier-transform infrared (FTIR) spectroscopy was performed on the samples using a PerkinElmer Spectrum 65 spectrometer. Before acquiring sample data, a background spectrum was recorded. The sample spectra were measured at room temperature with a scanning range of 4000–600 cm^{-1} and a resolution of 4 cm^{-1} across 32 scans. Each sample underwent three scans under the same conditions.

Water content percentages (WC%) of the hydrogels were determined using:

$$WC = \frac{W_h - W_x}{W_x} \times 100 \quad (2)$$

where W_h and W_x are the weights of the hydrogels and xerogels, respectively. In addition, the swelling degree (SD) was calculated using:

$$SD = \frac{W_s - W_x}{W_x} \times 100 \quad (3)$$

where W_s is the weight of the swollen samples. The swollen samples were prepared by immersing 1.0 g of xerogel in distilled water at room temperature. The swollen samples were removed, patted dry with absorbent paper, and weighed, after specific time intervals. The measurements continued until the swollen gel's weight stabilized, indicating that equilibrium swelling had been reached. The equilibrium swelling degree was defined as the plateau value in the swelling ratio *versus* time curve.

Mechanical and electrical tests were performed using a Mach-1 V500csst MA009 mechanical tester (Biomomentum Inc., Canada). Uniaxial tensile tests were performed on xerogel fibers to evaluate their mechanical response, using a constant crosshead speed of 30 mm min^{-1}. For xerogel fibers, a custom double-needle tensile mounting approach was used to enable reliable handling of small-diameter filaments (Fig. S1). Briefly, two syringe needle tips were positioned facing each other on the bench and separated by a predefined gauge gap of ~10 mm. The xerogel fiber was carefully threaded through both needle tips, and a single drop of cyanoacrylate adhesive was applied within the plastic cavity of each needle to immobilize the filament ends. The two needle tips were then seated onto a double-needle tip holder assembly (provided by Biomomentum Inc., Canada) designed for the Mach-1 tester. A 70 N load cell was used for these experiments. The holders were mounted coaxially, facing each other at the center of the testing chamber, and the double-needle assembly was firmly inserted onto the holders to establish a stable tensile configuration for fiber testing.

Electrical conductivity measurements were carried out using a tailored tensile grip with electrodes (model MA068) made by Biomomentum Inc., interfaced with a source measure unit (B2902A, Agilent). For all electrical measurements, copper tape was used to tab the xerogel fibers at both ends to ensure stable electrical contact between the sample and the electrodes. The electrical resistance of the samples was measured using the source measure unit during the test. The conductivity (σ, S m^{-1}) was calculated using:

$$\sigma = \frac{L}{R \times A} \quad (4)$$

where R denotes the average resistance (Ω), and L and A are the length (m) and cross-sectional area (m^2) of the xerogels between two grips, respectively. The reported conductivity values correspond to the average of 3 measurements, with error bars representing the standard deviation. Electrical continuity was further demonstrated by incorporating the xerogel conductor into a simple circuit connected to a light-emitting diode (LED), where successful illumination confirmed effective charge transport through the material.

The electromechanical response was evaluated by monitoring the relative resistance change ($\Delta R/R_0$) during tensile deformation using the same mechanical testing system coupled to the source measure unit. The relative resistance change was defined as:

$$\frac{\Delta R}{R_0} = \frac{R - R_0}{R_0} \times 100 \quad (5)$$

where R is the instantaneous resistance and R_0 is the initial resistance at 0% strain. Additionally, the gauge factor (GF), indicating the sensitivity of the xerogel, was calculated using the following equation:

$$GF = \frac{\frac{\Delta R}{R_0}}{\varepsilon} \quad (6)$$

where ε represents the applied strain.

Humidity-dependent electrical measurements were performed using a Burnsco environmental chamber (ON, Canada). The relative humidity was incrementally increased, and samples were equilibrated at each humidity level for 30 min prior to conductivity measurements, which were carried out using the same electrode grips as described previously, connected to a source measure unit.

For wearable sensing demonstrations (refer to the results and discussion section for details), PPG-0.1 M borax xerogel fibers were placed on the skin and secured using a thin cured

Ecoflex elastomer film. Copper tape was applied at both ends of the fiber to establish electrical connections to the source measure unit, and the real-time resistance was recorded during human motion. All measurements were performed under ambient laboratory conditions (temperature ~22 °C, relative humidity ~20%).

Results and discussion

Preparation of PVA–PEDOT:PSS–Gly–borax hydrogels and xerogels

Here, we introduce a reinforced xerogel fiber strategy based on a double network of physically and dynamically crosslinked PVA–PEDOT:PSS, enabling mechanically robust, stable sensing materials. Fig. 1 illustrates the fabrication process and structural evolution of the xerogel fibers. A homogeneous aqueous solution of PVA, glycerol, and PEDOT:PSS was subjected to freeze–thaw cycling to induce physical crosslinking through the formation of PVA crystallite, producing free-standing hydrogels. Freezing drives phase separation and chain packing, generating crystalline junctions within a three-dimensional network that balance strength and elasticity. Although glycerol can participate in hydrogen bonding with PVA, substantial concentrations are typically required to markedly alter the hydrogen-bonded network.[39,40] In the present system, glycerol primarily acts as a plasticizer, improving chain mobility and flexibility within the matrix, while also acting as an electrical conductivity enhancer.[41,42] PEDOT:PSS provides the conductive phase. To further reinforce the network, the hydrogels were post-treated with sodium tetraborate decahydrate (borax), which forms borate–diol crosslinks with PVA chains.[43] This process yields mechanically robust and conductive double-network xerogel fibers.

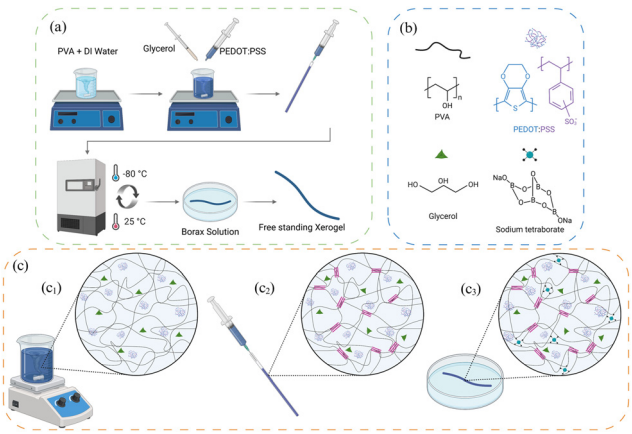

Fig. 1 (a) Schematic illustration of the fabrication process of the xerogels. (b) Chemical structures of PVA, glycerol, sodium tetraborate (borax), and PEDOT:PSS. (c) Schematic representation of the network evolution during processing: (c_1) homogeneous precursor solution after mixing, (c_2) physically crosslinked network formed *via* freeze–thaw cycling, and (c_3) chemically crosslinked network after borax treatment. Schematic created with BioRender.

Scanning electron microscopy was used to examine the fracture morphology of the xerogels prepared under different conditions (Fig. 2a–c). The cast-only sample exhibited a featureless fracture surface, indicating a dense and relatively homogeneous polymer network formed in the absence of any crosslinking. In contrast, the PVA–PEDOT:PSS–glycerol freeze–thaw sample (PPG) exhibited a textured fracture surface, reflecting the porous network typically formed in hydrogels during freeze–thaw gelation, where subsequent dehydration leads to partial pore collapse.[44–46] Following borax treatment, the PPG-0.1 M borax xerogel displayed an even more textured morphology, suggesting further modification and reinforcement of the network due to the formation of the double-network structure.

FTIR spectra of the cast-only sample (PPG-CO), freeze–thaw xerogel (PPG), and borax-treated xerogels (0.1–0.5 M) are shown in Fig. 2d. The broad absorption band at 3000–3600 cm^{-1} is attributed to the stretching vibration of hydroxyl (–OH) groups in PVA.[47–49] The peak at 2915 cm^{-1} corresponds to the stretching vibration of $-CH_2$ groups.[50] The characteristic band at 1000–1150 cm^{-1} (ref. 50 and 51) is associated with C–O stretching and crystalline domains of PVA. Additionally, the asymmetric stretching vibration of B–O–C at 1415 cm^{-1} confirms the crosslinking of PVA with borate ions through the formation of tetrahedral complexes.[52]

Thermogravimetric analysis (Fig. S2) was conducted to evaluate the thermal stability of the xerogels before and after borax treatment. Both samples exhibited minimal mass loss below 150 °C, indicating a negligible amount of residual free water. The untreated PPG sample showed the onset of major weight loss at around 200 °C, whereas the borax-crosslinked xerogel exhibited a delayed degradation onset, indicating enhanced thermal stability due to the formation of additional crosslinks, consistent with previous reports.[53] The primary degradation stage between 300 and 500 °C corresponds to decomposition of the PVA backbone and PEDOT:PSS.[54,55] Notably, the borax-treated sample displayed a higher residual mass at elevated

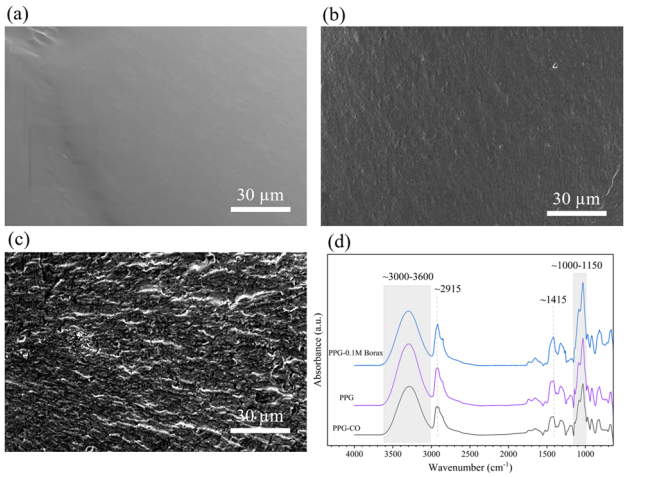

Fig. 2 (a)–(c) SEM images showing the fracture morphology of (a) CO-PPG, (b) PPG, and (c) PPG-0.1 M borax xerogels. (d) FTIR spectra of the CO-PPG film, PPG xerogel film, and PPG-0.1 M borax xerogel film.

temperatures, confirming the formation of a more thermally stable network. These results demonstrate that borax treatment effectively improves the thermal resistance of the xerogel by increasing the crosslink density.

Differential scanning calorimetry (DSC) thermograms obtained during the second heating cycle are shown in Fig. S3a. The untreated PPG sample exhibited no distinct melting transition, indicating that crystalline domains formed during freeze–thaw processing were either thermally unstable or highly constrained. This behavior can be attributed to the presence of physical crosslinks formed during freeze–thaw processing, which restrict the mobility of amorphous chain segments and inhibit the formation of well-defined crystalline domains detectable during the second heating cycle.[56] In contrast, borax-treated xerogels displayed a pronounced endothermic peak at approximately 160–190 °C, corresponding to the melting of crystalline domains formed within the more constrained network. The degree of crystallinity (Fig. S3b) increased progressively with borax concentration, confirming that borax treatment promotes structural ordering. Additionally, the melting peak broadened with increasing borax concentration, indicating a wider distribution of crystalline domain sizes. This broadening is attributed to reduced chain mobility caused by borate crosslinks, which disrupt uniform crystal growth and lead to crystals with varying sizes and stability.[57]

Swelling behavior

To evaluate the structural stability of the developed materials and to gain insight into the internal double-network architecture, the dehydration and swelling behaviors were investigated. For these swelling studies, samples were prepared as films using small square molds to obtain specimens with uniform geometry. Swelling analysis provides information about the internal polymer structure and crosslinking density, reflecting the relationship between network organization and water transport properties. Fig. 3a shows representative photographs of the hydrogel, the corresponding xerogel after drying, and the swollen sample after rehydration. Fig. 3b shows the temporal evolution of water content during ambient drying. All compositions exhibit a continuous and nearly linear decrease in water content, reaching near-complete dehydration and equilibrium with ambient humidity within approximately 8 hours. The similar drying profiles observed for all samples indicate that borax treatment does not significantly alter the overall evaporation kinetics.

In contrast, the swelling behavior was strongly influenced by borax concentration (Fig. 3c and d). Borax-treated xerogels exhibited faster swelling kinetics and higher equilibrium swelling degrees compared to the untreated PPG sample. The influence of borax on swelling in PVA-based systems is not universal, as both decreases[57–59] and increases[60–62] in swelling have been reported depending on network structure and processing conditions. In PVA networks crosslinked solely by borax, borax crosslinks often restrict chain mobility and reduce swelling. However, in the present freeze–thaw-derived network, borax treatment increases swelling capacity. This behavior

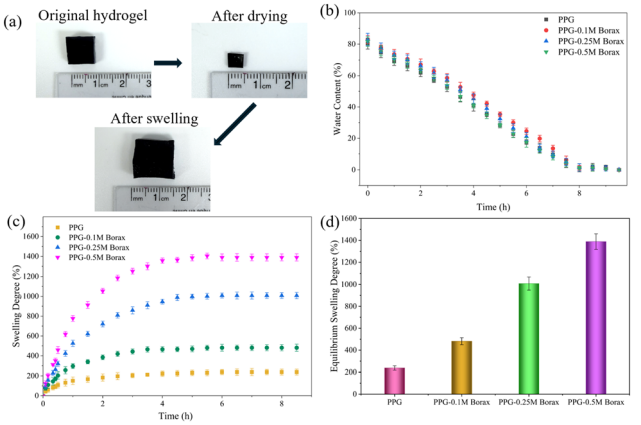

Fig. 3 (a) Digital images of the PPG-0.1 M borax hydrogel, the same sample after drying, and after swelling in water for 4 h. (b) Dehydration behavior of PPG and borax-treated xerogels (0–0.5 M) under ambient conditions, showing water content as a function of drying time until equilibrium with ambient humidity. (c) Swelling kinetics in deionized water, where samples were periodically weighed to determine swelling degree over time. (d) Equilibrium swelling degree of xerogels treated with different borax concentrations after reaching mass stabilization in water. Data represent mean ± standard deviation (n = 3).

likely arises from the interaction between borate ions and hydroxyl groups on PVA chains, which modifies the original hydrogen-bonding network formed during freeze–thaw gelation. The formation of borate crosslinks partially disrupts locally dense hydrogen-bonded regions, leading to a more open network structure that facilitates water penetration. As a result, the equilibrium swelling degree increases with borax concentration, reflecting greater water uptake within the double-network xerogel.

Appropriate swelling ability is important for sensing and bioelectronics applications, as it influences fluid transport, interfacial contact, and material stability in aqueous environments. Similar PVA–borax systems reported in the literature exhibit swelling ratios ranging from ~32% to 600%, demonstrating suitability for applications such as wound dressings and soft sensors.[58,59,63,64] The swelling performance achieved here falls within this range, highlighting the suitability of these double network xerogel fibers for aqueous and bioelectronic applications.

Mechanical properties

The tensile behavior of the xerogel fibers was evaluated using a custom double-needle tensile mounting system (Fig. 4a) designed to securely hold soft and compliant fibers without inducing stress concentrations or slippage. In this configuration, each fiber was fixed inside opposing syringe needle tips using adhesive and mounted onto the tensile tester. Representative stress–strain curves under tensile loading are shown in Fig. 4b. The curves are representative of three independent measurements, with statistical analysis presented in Fig. 4c and d. Compared to the freeze–thaw-only PPG fibers, borax-treated samples displayed higher stress levels across the entire strain range, indicating effective reinforcement of the network.

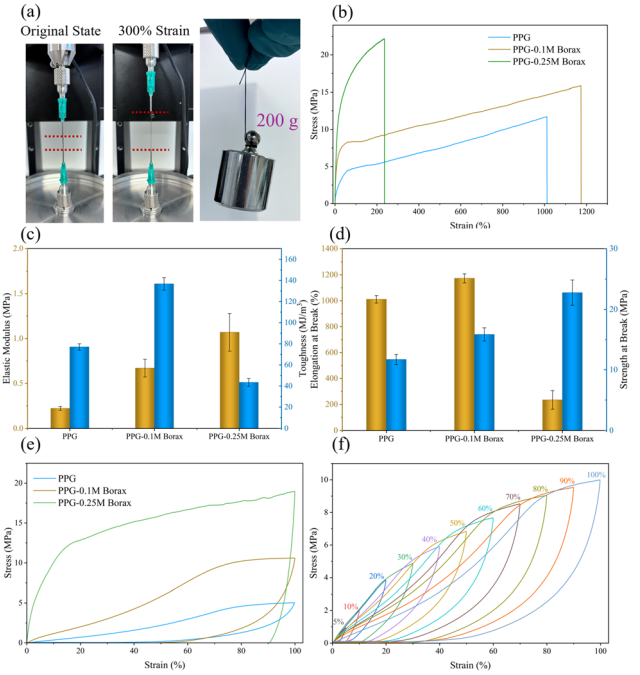

Fig. 4 (a) Digital images of a PPG-0.1 M borax xerogel fiber during tensile testing, showing the original state and elongation to 300% strain (the red dashed lines indicate the gauge region of the fiber between the tensile grips), along with a demonstration of load-bearing capability (200 g). (b) Representative tensile stress–strain curves. (c) Elastic modulus and toughness (mean ± SD, n = 3). (d) Elongation at break and strength at break (mean ± SD, n = 3). (e) Loading–unloading tensile curves of PPG xerogels with 0, 0.1 M, and 0.25 M borax. (f) Cyclic tensile behavior of PPG-0.1 M borax fibers at increasing strain levels (5–100%).

Quantitative analysis further confirms this trend (Fig. 4c and d). The elastic modulus, extracted from the slope of the initial linear region of the stress–strain curves (0–10% strain), increased substantially with borax concentration, reflecting the introduction of additional borate–diol interactions that strengthen the polymer network. The modulus increased by more than 4.5 times from the untreated PPG sample to the 0.25 M borax-treated xerogel, consistent with the increased effective crosslink density widely reported in PVA–borax systems.[66,67] Similarly, the tensile strength at break increased progressively with borax concentration, approximately doubling from the untreated PPG sample to the 0.25 M borax-treated xerogel, demonstrating improved load-bearing capacity and tunable mechanical properties through borax-mediated crosslinking. The tensile strength achieved here is comparable to or higher than previously reported PVA-based fibers while maintaining similar to higher stretchability.[36,37]

The enhanced mechanical performance of the xerogel fibers can be attributed to the synergistic effect of the double-network structure. The freeze–thaw process induces the formation of physically crosslinked PVA crystalline domains, which act as elastic junction points and provide an initial load-bearing network.[24] Subsequent borax treatment introduces borate–diol interactions, increasing the effective crosslink density and reinforcing the network.[65] This combination enables efficient stress distribution during deformation, where the physical network contributes to elasticity while the borate crosslinks provide additional resistance to deformation and energy dissipation. As a result, the xerogel fibers exhibit both high tensile strength and large extensibility.

The elongation at break initially increased at moderate borax concentration (0.1 M) but decreased at higher concentration (0.25 M). At moderate borax content, additional borate–diol interactions reinforce the network while still allowing sufficient chain mobility, leading to improved extensibility. At higher borax concentration, the increased crosslink density imposes stronger network constraints, restricting chain mobility and resulting in more brittle behavior. This trend highlights the intrinsic trade-off between mechanical reinforcement and flexibility, where increased crosslink density enhances stiffness and strength but limits extensibility.[79] The toughness followed a similar trend, reaching a maximum (136.78 ± 5.95 MJ m^{-3}) at intermediate borax concentration before decreasing at higher borax concentration, indicating an optimal crosslinking window at moderate borax concentration, beyond which excessive crosslinking windows where the balance between strength and extensibility maximizes energy dissipation.

Subsequently, cyclic tensile tests were conducted to assess the energy dissipation behavior of the xerogel fibers (Fig. 4e). All samples exhibit evident hysteresis loops during loading–unloading, and the loop area increases with borax concentration (PPG < PPG-0.1 M < PPG-0.25 M). The enlarged hysteresis indicates greater mechanical energy dissipation, consistent with a more highly crosslinked network that increases internal friction and limits molecular rearrangement during deformation. These results further support that borax post-treatment strengthens the double-network structure by increasing crosslink density, leading to improved mechanical robustness and toughness. Overall, our xerogel fibers exhibited higher ultimate stress and strain than many previously reported PVA-based strain sensors (Table 1). As summarized in Table 1, many reported PVA-based strain sensors exhibit elongations at break in the range of a few hundred percent, whereas the present xerogel fibers reach over 1100% strain while maintaining high tensile strength. This combination highlights the ability of the double-network xerogel structure to achieve unusually large deformation without sacrificing mechanical robustness.

To further evaluate mechanical stability, cyclic tensile tests at progressively increasing strain were performed on the PPG-0.1 M borax fibers, corresponding to the optimal crosslink density (Fig. 4f). As the applied strain increased from 5% to 100%, the hysteresis loops progressively expanded and the maximum stress increased steadily, demonstrating stable load-bearing capability and mechanical integrity, consistent with previous reports.[80–82] The well-defined, closed loops indicate that the fibers maintain structural integrity throughout the loading–unloading cycles, confirming that borax post-treatment produces a mechanically robust network capable of sustaining repeated deformation without failure. This combination of high stretchability and mechanical robustness is

Table 1 Comparison of properties of recent PVA-based strain sensors

Material	Fabrication method	Conductivity (S m^{-1})	Strength (MPa)	Strain (%)	Ref.
PVA–HPC	Salt solution soaking	3.4	1.3	975	68
PVA–TA@talc	Molecular-level ion conductive channels + F–T	1.7	∼0.7	∼750	69
PVA–PEDOT:PSS–Gly	F–T	0.163	13.76	519.9	37
PVA–PA	Hot-pressing + F–T	—	∼0.7	>1000	70
PVA	Crosslinking with alkaline metal hydroxide	—	∼13	∼350	71
PVA–Mxene–PEDOT:PSS–PDA	Dynamic supramolecular cross-linking	—	∼1 N	∼700	72
PVA–HGNs	Doping nanofillers + directional freezing + salting out	2.8	9.5	2058	36
PVA–SL	Cross-linking with sodium lignosulfonate	—	∼6	571	73
PVA–PEDOT:PSS–DMSO–borax	Physical crosslinking + borax crosslinking	—	∼0.23	∼300	74
PVA–SA–PESOT:PSS–$ZnSO_4$	F–T + salting-out	3.75	34.22	402	75
PVA–IL–borax	Borax crosslinking + F–T	3.25	3.1	∼500	76
PVA–CS–glycerol	One-pot synthesis + F–T	0.95	6.29	497	77
PVA/Gly-LNM/CNCs/PEDOT:PSS	Solution blending + F–T	—	∼65	320	78
PVA–PEDOT:PSS–glycerol–borax	F–T + borax crosslinking	0.8	15.85 ± 1.12	1173.02 ± 33.21	This work

particularly advantageous for strain sensing applications, where large deformation and repeated loading are required. As summarized in Table 1, the present xerogel fibers combine high tensile strength (∼16 MPa) and large elongation (>1100%) with conductivity in the typical range of PVA-based strain sensors. While some systems achieve higher conductivity or sensitivity, they often do so at the expense of mechanical robustness or stretchability. In contrast, the present system provides a balanced combination of mechanical and electromechanical performance in a water-independent xerogel format.

Electromechanical properties

Charge transport in the xerogel fibers occurs through a combination of continuous PEDOT:PSS pathways and interdomain hopping/tunneling between conductive regions embedded within the PVA matrix. PEDOT:PSS endows the xerogel fibers with electrical conductivity by forming a continuous conductive network. All samples exhibited similar conductivities of approximately 0.8 S m^{-1}, indicating that the freeze–thaw process and borax crosslinking did not significantly disrupt electrical pathways. The moderate conductivity is likely due to the high fraction of insulating PVA and the dense xerogel network formed after drying, which favors mechanical robustness and structural stability over maximization of electrical transport. As summarized in Table 1, most reported PVA-based strain sensors exhibit conductivities in the range of ∼0.1 to a few S m^{-1}. The conductivity of the present xerogel fibers falls within this range, reflecting a balance between electrical performance and mechanical robustness. This reflects a trade-off between mechanical robustness and electrical transport, as increased crosslinking and PVA content reduce the connectivity of PEDOT:PSS pathways. The electrical stability of the PPG-0.1 M borax fibers under deformation was qualitatively demonstrated using a simple LED circuit (Fig. 5a). The LED remained illuminated when the fiber was stretched up to 200% strain, confirming the preservation of conductivity during large deformation, although its brightness gradually decreased due to the strain-induced increase in resistance.

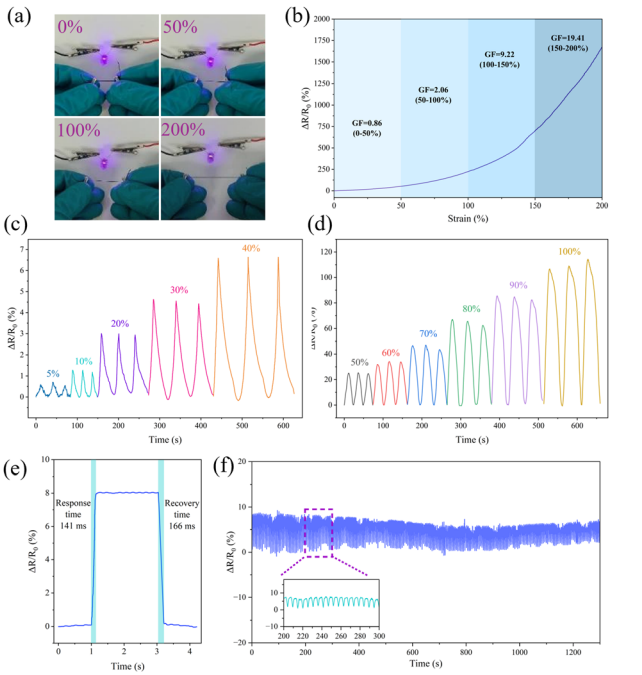

Fig. 5 (a) Digital images of the strain sensor at 0%, 50%, 100%, and 200% tensile strain, demonstrating stable electrical response during deformation. (b) Relative resistance change ($\Delta R/R_0$) as a function of strain, with calculated gauge factors in different strain regions. Variation in relative resistance of the xerogel fibers in response to (c) small strains (5–40%) and (d) large strains (50–100%). (e) Response time and recovery time of the PPG-0.1 M fiber under 40% strain. (f) Cyclic electromechanical response of the PPG-0.1 M borax xerogel fiber during 300 stretching cycles at 30% strain, demonstrating signal stability.

To quantitatively characterize this behavior, the relative resistance change ($\Delta R/R_0$) was measured as a function of tensile strain (Fig. 5b). The relative resistance increased progressively with increasing strain, confirming that the xerogel fibers are suitable for use as strain sensors. The gauge factor (GF), calculated from the slope of the relative resistance–strain curve, remained modest at 0.86 and 2.06 in the 0–50% and 50–100%

strain ranges, respectively, before increasing sharply to ~9 and ~19 at higher strains (100–150% and 150–200%). At low strain, the conductive PEDOT:PSS network deforms elastically together with the PVA matrix, and the resistance change is mainly governed by geometric effects, including elongation of the conductive pathway and reduction of the cross-sectional area. As the strain increases, the distance between PEDOT-rich conductive regions within the polymer network gradually increases, which reduces interchain contact and increases charge transport resistance through hopping or tunneling mechanisms. At larger strains, continued stretching of the polymer network further increases the transport distance between conductive pathways, leading to a more pronounced resistance increase and the sharp rise in gauge factor observed at higher strain.[83,84] At low strain (<100%), these gauge factor values are consistent with those reported for similar strain sensors, which typically remain below ~3. At higher strains (100–200%), the xerogel fibers exhibit significantly enhanced sensitivity, surpassing commonly reported values in the literature (typically ~3–5).[37,81,85,86]

The electrical response of the xerogel fibers under cyclic deformation was evaluated at different strain levels (Fig. 5c and d). The fibers exhibited stable and repeatable resistance changes over multiple loading–unloading cycles, with the signal amplitude increasing systematically with increasing strain. Distinct and well-defined responses were observed even at low strains, while larger strains produced proportionally greater resistance variations. The consistent signal profiles and clear differentiation between strain levels demonstrate the reliability and sensitivity of the xerogel fibers for repeated strain sensing. Furthermore, the response time of the PPG-0.1 M borax xerogel fiber was evaluated under dynamic deformation at 40% strain. The sensor exhibits a rapid electrical response, with a response and recovery time in the range of 100–200 ms, indicating fast and reliable signal response. This response time is comparable to typical polymer-based strain sensors, indicating fast and reliable signal response.

The electromechanical stability of the xerogel fibers was further evaluated during 300 consecutive loading–unloading cycles at 30% strain, where the resistance signal remained stable and reproducible with no noticeable drift or degradation (Fig. 5f). The consistent peak amplitudes and waveform profiles indicate that the conductive network remains intact during repeated deformation. This stable electrical performance highlights the robustness of the xerogel fibers and their suitability for reliable strain sensing under repeated mechanical loading. Compared with previously reported hydrogel/xerogel strain sensors, which are often assessed over 100–600 cycles and sometimes higher, our xerogel fibers show comparable cyclic stability.[37,86]

The effect of environmental humidity on the electrical conductivity of the xerogel fibers was investigated over a relative humidity range of approximately 25% to 95% (Fig. S4). As the relative humidity increased, the conductivity exhibited a gradual rise from ~0.8 S m^{-1} to ~1.6 S m^{-1}, corresponding to an approximately twofold increase. This behavior is likely attributed to moisture uptake within the PVA-based matrix, which enhances polymer chain mobility and can facilitates charge transport through the PEDOT:PSS network. In addition, the presence of absorbed water may contribute to ionic conduction, further increasing the overall conductivity.[87,88] Despite this increase, the conductivity remains within the same order of magnitude across the full humidity range, indicating relatively stable electrical performance under varying environmental conditions.

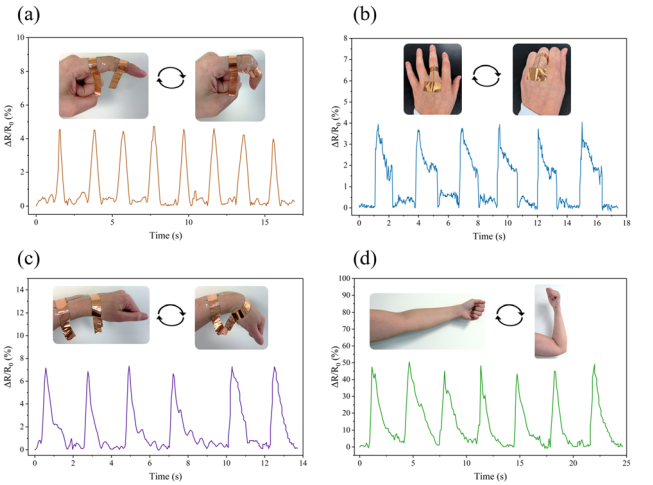

Fig. 6 Real-time relative resistance changes of the xerogel fibers during human motion monitoring: (a) finger bending, (b) fist clenching, (c) wrist bending, and (d) elbow bending.

Application of xerogel fibers in motion monitoring

To evaluate the ability of the xerogel fibers to monitor human motion, the sensors were attached to different body locations for dynamic testing (Fig. S5 and Fig. 6). When mounted on the finger, the sensor produced distinct and repeatable resistance peaks corresponding to bending and releasing motions (Fig. 6a). Similarly, clear and stable electrical responses were observed during hand opening and closing, with consistent signal amplitudes and good reproducibility over multiple cycles (Fig. 6b). When positioned on larger joints such as the wrist and elbow, the fibers generate significantly higher resistance changes due to the greater deformation associated with these movements (Fig. 6c and d). Upon release of each movement, the signal rapidly returned to its baseline value, indicating fast recovery, good repeatability, and stable electrical performance. These results demonstrate the capability of the xerogel fibers to reliably monitor both subtle and large-scale human motion, highlighting their potential for wearable strain sensing applications.

Conclusions

In summary, we developed highly stretchable and conductive double-network PEDOT:PSS xerogel fibers through freeze–thaw processing followed by borax-mediated crosslinking. By varying the borax concentration, the mechanical properties of the

fibers could be systematically tuned. The combined physical and chemical crosslinking strategy produced mechanically robust fibers with elastic moduli ranging from ~0.2 to ~1 MPa and tensile strengths of ~12 to ~23 MPa, while maintaining elongation at break exceeding 1100%, demonstrating an effective balance between strength and extensibility. The xerogel fibers exhibited stable electrical conductivity and reproducible strain-dependent resistance changes with gauge factors ranging from 0.86 to ~19, along with excellent durability under repeated deformation. When integrated as wearable sensors, the fibers enabled reliable real-time monitoring of human motion. These results demonstrate that double-network conductive xerogel fibers provide a promising platform for mechanically robust and reliable wearable strain sensors. While the present study demonstrates promising performance, future work should include controlled mechanical testing under varying humidity conditions, particularly to investigate the coupled mechanical and electromechanical behavior under controlled humidity environments. In addition, systematic optimization of fiber geometry may further enhance the electromechanical performance of these xerogel fibers.

Author contributions

Gayaneh Petrossian: conceptualization, data curation, formal analysis, methodology, investigation, visualization, writing – original draft. Sara Ebrahimi: methodology, writing – review & editing. Floriane Miquet-Westphal: methodology, writing – review & editing. Hang Xu: supervision, validation, writing – review & editing. Fabio Cicoira: project administration, resources, supervision, validation, writing – review & editing.

Conflicts of interest

There are no conflicts to declare.

Data availability

The data supporting this study are openly available in Zenodo at https://doi.org/10.5281/zenodo.19742188. Supplementary information: includes additional experimental details and characterization results, including the tensile testing setup for the xerogel fibers, thermogravimetric analysis (TGA), differential scanning calorimetry (DSC) thermograms and crystallinity analysis, and photographs demonstrating the wearable strainsensing configuration. See DOI: https://doi.org/10.1039/d6ma00373g.

Acknowledgements

This research was supported by the Natural Science and Engineering Research Council of Canada (NSERC) through Discovery Grants awarded to FC (grant no. RGPIN-2025-05607) and HX (grant no. RGPIN-2024-06567). The equipment and infrastructure used in this study were acquired and maintained by the Canada Foundation for Innovation, FRQNT and NSERC. GP acknowledges support from the NSERC Vanier Canada Graduate Scholarship. S. E. and F. M. W. acknowledge the Fonds de recherche du Québec – Nature et technologies (FRQNT) for a Doctoral Scholarship. F. M.-W. acknowledge the support of Hydro-Québec, Fondation Arbour, and the Club Saint-Denis and Foundation and Alumni of Polytechnique Montreal for an Excellence Award scholarship. The protocol for human experiments was approved by the research ethics board of Polytechnique Montreal (certificate CER-2021-04-D), in accordance with the Tri-Council Policy Statement: Ethical Conduct for Research Involving Humans (TCPS). Written consent was obtained from the participant. The authors acknowledge the use of https://BioRender.com to create the schematics used in Fig. 1 (Petrossian, G. (2026) https://BioRender.com/tyscmea).

References

1 Y. Liu, H. Wang, W. Zhao, M. Zhang, H. Qin and Y. Xie, *Sensors*, 2018, **18**, 645.
2 A. Yu, M. Zhu, C. Chen, Y. Li, H. Cui, S. Liu and Q. Zhao, *Adv. Healthcare Mater.*, 2024, **13**, 1–21.
3 J. Li, Z. Fang, D. Wei and Y. Liu, *Adv. Healthcare Mater.*, 2024, **2401532**, 1–37.
4 Y. Lu, G. Yang, S. Wang, Y. Zhang, Y. Jian, L. He, T. Yu, H. Luo, D. Kong, Y. Xianyu, B. Liang, T. Liu, X. Ouyang, J. Yu, X. Hu, H. Yang, Z. Gu, W. Huang and K. Xu, *Nat. Electron.*, 2024, **7**, 51–65.
5 F. Lin, W. Yang, B. Lu, Y. Xu, J. Chen, X. Zheng, S. Liu, C. Lin, H. Zeng and B. Huang, *Adv. Funct. Mater.*, 2024, **2416419**, 1–16.
6 S.-H. Sunwoo, S. I. Han, C. S. Park, J. H. Kim, J. S. Georgiou, S.-P. Lee, D.-H. Kim and T. Hyeon, *Nat. Rev. Bioeng.*, 2024, **2**, 8–24.
7 M. Wang, T. Wang, Y. Luo, K. He, L. Pan, Z. Li, Z. Cui, Z. Liu, J. Tu and X. Chen, *Adv. Funct. Mater.*, 2021, **31**, 1–13.
8 K. K. Kim, Y. Suh and S. H. Ko, *Adv. Intell. Syst.*, 2021, **3**, 2000157.
9 L. Wang, F. Wei, Z. Zhai, R. Zhang, W. Liu and Z. Zhao, *Sens. Actuators, A*, 2024, **365**, 114909.
10 W. Heng, S. Solomon and W. Gao, *Adv. Mater.*, 2022, **34**, 1–48.
11 N. A. Shahrim, Z. Ahmad, A. Wong Azman, Y. Fachmi Buys and N. Sarifuddin, *Mater. Adv.*, 2021, **2**, 7118–7138.
12 N. Kim, S. Lienemann, I. Petsagkourakis, D. Alemu Mengistie, S. Kee, T. Ederth, V. Gueskine, P. Leclère, R. Lazzaroni, X. Crispin and K. Tybrandt, *Nat. Commun.*, 2020, **11**, 1424.
13 C. Volkert, M. Brzezinski, P. G. Argudo, R. Colucci, S. H. Parekh, P. Besenius, J. J. Michels and U. Kraft, *Adv. Sci.*, 2025, **2502853**, 1–9.
14 K. Pattanarat, N. Petchsang, T. Osotchan, Y. H. Kim and R. Jaisutti, *ACS Appl. Mater. Interfaces*, 2021, **13**, 48053–48060.
15 S. Ichikawa and N. Toshima, *Polym. J.*, 2015, **47**, 522–526.

16 Q. Liu, J. Qiu, C. Yang, L. Zang, G. Zhang and E. Sakai, *Adv. Mater. Technol.*, 2021, **6**, 1–11.
17 J. Kim, J. Fan, G. Petrossian, X. Zhou, P. Kateb, N. Gagnon-Lafrenais and F. Cicoira, *Mater. Horiz.*, 2024, **11**, 3548–3560.
18 P. Kateb, J. Fan, J. Kim, X. Zhou, G. A. Lodygensky and F. Cicoira, *Flexible Printed Electron.*, 2023, **8**, 045006.
19 Y. Wang, C. Gao, C. Zhao, Z. Chen, H. Ye, M. Shen, Q. Gao, J. Zhu and T. Chen, *ACS Appl. Mater. Interfaces*, 2023, **15**, 17175–17187.
20 C. I. Idumah, J. H. Low and E. O. Emmanuel, *Polym. Bull.*, 2023, **80**, 11557–11587.
21 W. Hu, Z. Wang, Y. Xiao, S. Zhang and J. Wang, *Biomater. Sci.*, 2019, **7**, 843–855.
22 H. Chamkouri, *Am. J. Biomed. Sci. Res.*, 2021, **11**, 485–493.
23 W. X. Waresindo, H. R. Luthfianti, A. Priyanto, D. A. Hapidin, D. Edikresnha, A. H. Aimon, T. Suciati and K. Khairurrijal, *Mater. Res. Express*, 2023, **10**, 024003.
24 F. Wu, J. Gao, Y. Xiang and J. Yang, *Polymers*, 2023, **15**, 3782.
25 G. Mugnaini, R. Gelli, L. Mori and M. Bonini, *ACS Appl. Polym. Mater.*, 2023, **5**, 9192–9202.
26 A. Chang, Z. Ye, Z. Ye, J. Deng, J. Lin, C. Wu and H. Zhu, *Carbohydr. Polym.*, 2022, **291**, 119520.
27 X. Zhou, A. Rajeev, A. Subramanian, Y. Li, N. Rossetti, G. Natale, G. A. Lodygensky and F. Cicoira, *Acta Biomater.*, 2022, **139**, 296–306.
28 C. Liu, F. Lei, P. Li, K. Wang and J. Jiang, *Int. J. Biol. Macromol.*, 2021, **182**, 1179–1191.
29 S. Cho, S. Y. Hwang, D. X. Oh and J. Park, *J. Mater. Chem. A*, 2021, **9**, 14630–14655.
30 M. B. Lawrence, *Polym. Bull.*, 2024, **81**, 13783–13801.
31 J. Xu, X. Liu, X. Ren and G. Gao, *Eur. Polym. J.*, 2018, **100**, 86–95.
32 J. Hao and R. A. Weiss, *Polymer*, 2013, **54**, 2174–2182.
33 P. Wang, H. Zeng, J. Zhu and Q. Gao, *Chem. Eng. J.*, 2024, **484**, 149676.
34 H. Zeng, C. Gao, Y. Yu, M. Jiang, T. Deng and J. Zhu, *Acc. Mater. Res.*, 2025, **6**, 952–963.
35 Z. Chen, J. Chen, H. Ge, Q. Gao, J. Zhu, C. Zhu and C. Gao, *Chem. Eng. J.*, 2025, **518**, 164807.
36 Y. Zhou, Y. Mi, Y. Liu, X. Luo, N. Chen, L. Wang, C. Guo, W. Lv, B. Peng, Y. Niu and Q. Xu, *Appl. Mater. Today*, 2023, **34**, 101894.
37 W. Shi, Z. Wang, H. Song, Y. Chang, W. Hou, Y. Li and G. Han, *ACS Appl. Mater. Interfaces*, 2022, **14**, 35114–35125.
38 H. S. Bu, W. Aycock, S. Z. D. Cheng and B. Wunderlich, *Polymer*, 1988, **29**, 1485–1494.
39 S. Peng, S. Liu, Y. Sun, N. Xiang, X. Jiang and L. Hou, *Eur. Polym. J.*, 2018, **106**, 206–213.
40 S. Shi, X. Peng, T. Liu, Y.-N. Chen, C. He and H. Wang, *Polymer*, 2017, **111**, 168–176.
41 T. Yang, J. Wu, Y. Yao, K. Wang, Q. Zhang and Q. Fu, *Polymer*, 2024, **301**, 127031.
42 H. Li and M. A. Huneault, *J. Appl. Polym. Sci.*, 2011, **119**, 2439–2448.
43 H.-L. Lin, Y.-F. Liu, T. L. Yu, W.-H. Liu and S.-P. Rwei, *Polymer*, 2005, **46**, 5541–5549.
44 F. Soto-Bustamante, G. Bassu, E. Fratini and M. Laurati, *Gels*, 2023, **9**, 396.
45 R. Ricciardi, F. Auriemma, C. De Rosa and F. Lauprêtre, *Macromolecules*, 2004, **37**, 1921–1927.
46 A. Górska, E. Baran, J. Knapik-Kowalczuk, J. Szafraniec-Szczęsny, M. Paluch, P. Kulinowski and A. Mendyk, *Pharmaceutics*, 2024, **16**, 1388.
47 X. Qi, X. Yao, S. Deng, T. Zhou and Q. Fu, *J. Mater. Chem. A*, 2014, **2**, 2240–2249.
48 S. N. Kale, J. Mona, S. Dhobale, T. Thite and S. L. Laware, *J. Appl. Polym. Sci.*, 2011, **121**, 2450–2457.
49 G. Cai, J. Wang, K. Qian, J. Chen, S. Li and P. S. Lee, *Adv. Sci.*, 2017, **4**, 1600190.
50 X. Qi, X. Hu, W. Wei, H. Yu, J. Li, J. Zhang and W. Dong, *Carbohydr. Polym.*, 2015, **118**, 60–69.
51 C. M. Hassan and N. A. Peppas, *Biopolymers PVA Hydrogels, Anionic Polymerisation Nanocomposites*, Springer, Berlin, Heidelberg, 2000, pp. 37–65.
52 E. Al-Emam, H. Soenen, J. Caen and K. Janssens, *Heritage Sci.*, 2020, **8**, 106.
53 N. Q. Vu, T. M. Le, A. N. B. Ngo, M. H. T. Nguyen, Y.-C. Liao and T. T. Tran, *ACS Polym. Au*, 2026, **6**, 33–60.
54 J. L. Carter, C. A. Kelly and M. J. Jenkins, *Polym. J.*, 2023, **55**, 253–260.
55 D. A. Ahmad Ruzaidi, M. R. Maurya, S. Yempally, S. Abdul Gafoor, M. Geetha, N. Che Roslan, J.-J. Cabibihan, K. Kumar Sadasivuni and M. M. Mahat, *RSC Adv.*, 2023, **13**, 8202–8219.
56 B. Sreedhar, M. Sairam, D. K. Chattopadhyay, P. A. S. Rathnam and D. V. M. Rao, *J. Appl. Polym. Sci.*, 2005, **96**, 1313–1322.
57 M. Huang, Y. Hou, Y. Li, D. Wang and L. Zhang, *Des. Monomers Polym.*, 2017, **20**, 505–513.
58 O. Zandraa, F. A. Ngwabebhoh, R. Patwa, H. T. Nguyen, M. Motiei, N. Saha, T. Saha and P. Saha, *Int. J. Pharm.*, 2021, **607**, 120952.
59 W. Liu, C. Yao, D. Wang, G. Du, Y. Ji and Q. Li, *Gels*, 2024, **10**, 821.
60 Y. Qin, J. Wang, C. Qiu, X. Xu and Z. Jin, *J. Agric. Food Chem.*, 2019, **67**, 3966–3980.
61 K. Ingtipi, B. J. Choudhury and V. S. Moholkar, *Prog. Org. Coat.*, 2023, **174**, 107268.
62 C. Wang, Z. Shen, P. Hu, T. Wang, X. Zhang, L. Liang, J. Bai, L. Qiu, X. Lai, X. Yang and K. Zhang, *J. Sol-Gel Sci. Technol.*, 2022, **101**, 103–113.
63 J. Tavakoli and Y. Tang, *Mater. Sci. Eng., C*, 2017, **77**, 318–325.
64 L. Tu, Y. Fan, Y. Deng, L. Hu, H. Sun, B. Zheng, D. Lu, C. Guo and L. Zhou, *Molecules*, 2023, **28**, 1321.
65 J. Han, H. Wang, Y. Yue, C. Mei, J. Chen, C. Huang, Q. Wu and X. Xu, *Carbon*, 2019, **149**, 1–18.
66 A. Li, J. Zhang, M. A. A. Newton, Y. Liu, T. Li and B. Xin, *Polymer*, 2025, **337**, 129027.
67 A. Dixit and D. S. Bag, *Eur. Polym. J.*, 2022, **175**, 111347.
68 Y. Zhou, C. Wan, Y. Yang, H. Yang, S. Wang, Z. Dai, K. Ji, H. Jiang, X. Chen and Y. Long, *Adv. Funct. Mater.*, 2019, **29**, 1806220.

69 X. Pan, Q. Wang, R. Guo, Y. Ni, K. Liu, X. Ouyang, L. Chen, L. Huang, S. Cao and M. Xie, *J. Mater. Chem. A*, 2019, **7**, 4525–4535.
70 R. Hu, J. Zhao, Y. Wang, Z. Li and J. Zheng, *Chem. Eng. J.*, 2019, **360**, 334–341.
71 M. A. Darabi, A. Khosrozadeh, Y. Wang, N. Ashammakhi, H. Alem, A. Erdem, Q. Chang, K. Xu, Y. Liu, G. Luo, A. Khademhosseini and M. Xing, *Adv. Sci.*, 2020, **7**, 1902740.
72 W. Zhao, D. Zhang, Y. Yang, C. Du and B. Zhang, *J. Mater. Chem. A*, 2021, **9**, 22082–22094.
73 Q. He, L. Ren, J. Xu, N. Wu, L. Wang and W. Song, *ACS Appl. Polym. Mater.*, 2026, **8**, 2856–2868.
74 J. Cao, Z. Zhang, K. Li, C. Ma, W. Zhou, T. Lin, J. Xu and X. Liu, *Nanomaterials*, 2023, **17**, 2465.
75 Z. Cao, Z. Chen, Z. Li, Y. Zou, J. Guo, R. Guo, G. Liu, F. Zhou and W. Liu, *ACS Appl. Polym. Mater.*, 2026, **8**(4), 2598–2608.
76 M. Meng, R. Fu, T. Xue, X. Liu, J. Jiang and X. Liu, *Chem. Eng. J.*, 2025, **519**, 165709.
77 T. Wang, T. Yu, C. Jiang, Y. Yu, J. Fu, J. Zhu, Q. Zhang, J. Liang, Z. Xue, R. Li and G. Chang, *Compos. Struct.*, 2026, **382**, 120084.
78 S.-C. Shi, Y.-C. Hsieh and D. Rahmadiawan, *ACS Omega*, 2025, **10**, 14666–14675.
79 Y. Wang, P. Chen, Y. Ding, P. Zhu, Y. Liu, C. Wang and C. Gao, *Adv. Funct. Mater.*, 2024, **34**, 2409081.
80 L. Dai, Z. Zhou, Y. Chang, Z. Liu, J. Sun, C. Qin, J. Wang and L. Dai, *ACS Appl. Mater. Interfaces*, 2025, **17**, 59747–59758.
81 D. Bi, N. Qu, W. Sheng, T. Lin, S. Huang, L. Wang and R. Li, *ACS Appl. Mater. Interfaces*, 2024, **16**, 11914–11929.
82 Y. Zhang, Y. Wang, Y. Bao, B. Lin, G. Cheng, N. Yuan and J. Ding, *Colloids Surf., A*, 2024, **691**, 133833.
83 Y. Yang, G. Zhao, X. Cheng, H. Deng and Q. Fu, *ACS Appl. Mater. Interfaces*, 2021, **13**, 14599–14611.
84 R. Luo, X. Li, H. Li, B. Du and S. Zhou, *Prog. Org. Coat.*, 2022, **162**, 106593.
85 Z. Zhou, W. Yuan and X. Xie, *Mater. Chem. Front.*, 2022, **6**, 3359–3368.
86 Y. Gao, S. Gu, F. Jia and G. Gao, *J. Mater. Chem. A*, 2020, **8**, 24175–24183.
87 E. S. Muckley, C. B. Jacobs, K. Vidal, J. P. Mahalik, R. Kumar, B. G. Sumpter and I. N. Ivanov, *ACS Appl. Mater. Interfaces*, 2017, **9**, 15880–15886.
88 L. P. Kreuzer, M. Betker, M. Wolf, B.-J. Niebuur, J. Ollivier, L. D. Söderberg and S. V. Roth, *Macromolecules*, 2025, **58**, 2247–2258.